



Spectroscopic screening and performance parameters of hybrid perovskite ($\text{CH}_3\text{CH}_2\text{PH}_3\text{PbI}_3$) using WIEN2k and SCAPS-1d

Tarun Kumar Joshi ^a, Giriraj Sharma ^a, Yogita R. Sharma ^b, Ajay Singh Verma ^{c,d,*}

^a Department of Physics, Swami Vivekanand Govt. P.G. College, Neemuch, MP, 458441, India

^b Department of Mathematics, L.D. College of Engineering, Ahmedabad, 380015, India

^c Division of Research & Innovation, School of Applied and Life Sciences, Uttarakhand University, Dehradun, 248007, India

^d University Centre for Research & Development, Department of Physics, Chandigarh University, Mohali, Punjab, 140413, India

ARTICLE INFO

Keywords:

Band structure
Absorption coefficient
Power conversion efficiency
Fill factor
Quantum efficiency

ABSTRACT

Herein, we propose that the commonly used methylammonium cation (CH_3NH_3^+) in $\text{CH}_3\text{NH}_3\text{PbI}_3$ (MAPbI₃) be replaced with ethyl-phosphonium cation $\text{CH}_3\text{CH}_2\text{PH}_3^+$ (EP⁺), allowing stronger electronic coupling between the PbI₆ octahedra and the organic cation and thereby increasing its stability. This paper will examine EP⁺ based hybrid perovskite ($\text{CH}_3\text{CH}_2\text{PH}_3\text{PbI}_3$ or EPPbI₃) as an alternative absorber material for photovoltaic cells of high efficiency and that too at affordable processing costs. By using FP-LAPW + lo methodology as used in density functional theory (DFT), we have examined physical features such as the bandgap energy, distribution of valence electron density, DOS, and optical and thermodynamical coefficients. We also simulated the performance of solar cells by employing EPPbI₃ as PVA material using SCAPS-1D. The findings of the current study viz. an absorption coefficient surpassing 10^4 cm^{-1} , a direct forbidden energy gap of 1.388 eV and simulated PCE of 31.8%, is enough to support applicability EPPbI₃ perovskite as a PVA material.

1. Introduction

Researchers are exploring a variety of efficient and environmentally-safe alternative renewable energy sources to address the ever-increasing energy demands. Sunlight is one of the most promising options. Currently, the solar panel industry is dominated by PV systems based on expensive crystalline silicon [1–5]. However, if more affordable alternatives to PVA material become available, they could be critical in the creation of low-cost and efficient renewable energy sources that also benefit the environment. This resulted in a hunt for low-cost PVA materials with PCEs similar to silicon; this is the area of material science that attracts the interest of most scholars. In the last decade, HOIPs attracted considerable interest due to rapid decrease in processing costs and a significant rise in PCE, which is now close to silicon [6–8]. The crystal structure of these HOIPs is of the O²⁻X⁻ type in which O²⁻ is an organic cation, M²⁺ is a metallic cation and X⁻ is a halide anion. These HOIPs possess the rare combination of desirable optical and electronic properties, such as an appropriate direct bandgap [9], long diffusion lengths with high mobility of carriers [9,10], small non-radiative Auger recombination rate [11], and desirable light-collection and transport properties [12]. These perovskites are also inexpensive and could be one

of the best candidate materials for fabrication of efficient PV devices.

Although these newly developed perovskites have shown considerable promise, they also have significant disadvantages, including poor resistance to high temperatures, moisture, and extended exposure to solar radiation [13]. To improve the performance of MAPbI₃-based devices, numerous methods have recently been put forth. Though MAPbI₃ devices have improved in terms of performance, yet their stability has been severely constrained, making modeling of these devices crucial if one wants to comprehend how stability can be increased for optimum cell performance.

Many efforts have been undertaken to understand and improve the stability of hybrid perovskite. It is found that the perovskite films are stable in the absence of air or light. However, it becomes unstable when both air and light (with and without UV) are present. When hybrid perovskite is exposed to light and air, iodide anions are produced. These anions then transfer electrons to p-type species in the environment and create free radicals, which react with the organic cations by absorbing the acid protons and subsequently produce extremely volatile methylamine that makes the hybrid perovskite unstable [14]. It is also discovered that UV stability of MAPbI₃ perovskite solar cells can be significantly enhanced without much compromising on power

* Corresponding author. Division of Research & Innovation, School of Applied and Life Sciences, Uttarakhand University, Dehradun, Uttarakhand, 248007, India.
E-mail address: ajay.phy@rediffmail.com (A.S. Verma).

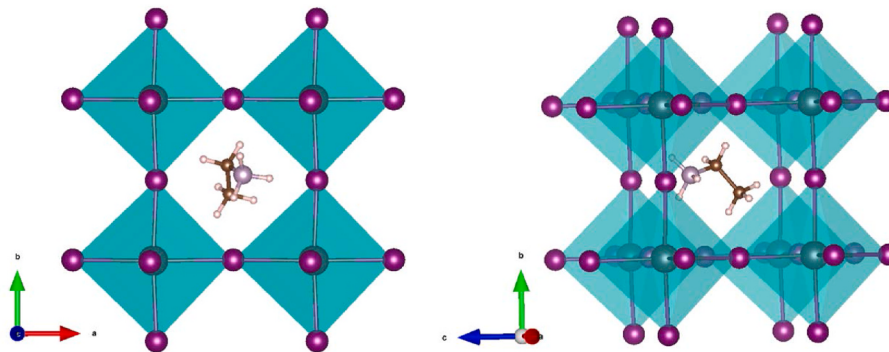


Fig. 1. The crystal structure of EPPbI₃ perovskite.

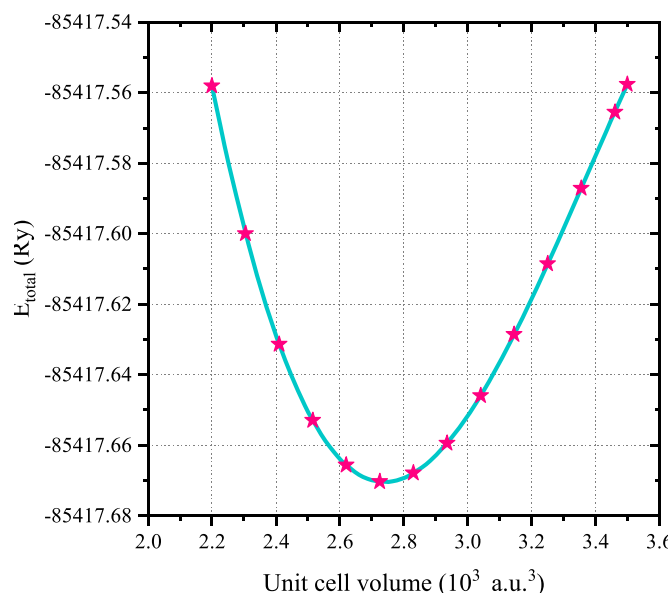


Fig. 2. The total energy E of the unit cell of the EPPbI₃ perovskite in terms of the unit cell volume V.

conversion efficiency by replacing 20% iodine with bromine [15–18].

Recently, it has been reported that replacing methyl-ammonium cation (CH_3NH_3^+) in $\text{CH}_3\text{NH}_3\text{PbI}_3$ or MAPbI₃ with phosphonium-based organic cation ($-\text{PH}_3^+$) allows stronger electronic coupling between the PbI₆ octahedra and the organic cation, thereby increasing its stability [19]. The higher the stability of lead-based halide perovskites, the lesser amount of lead would leak into the environment which would minimize its hazardous consequences. This motivates us to propose in this study, for the first time, that the methyl-ammonium cation (CH_3NH_3^+) in $\text{CH}_3\text{NH}_3\text{PbI}_3$ or MAPbI₃ be replaced by the molecular cation $\text{CH}_3\text{CH}_2\text{PH}_3^+$ (EP $^+$).

To thoroughly investigate the suitability of perovskite materials for solar cell applications, a detailed study of important parameters including the absorption coefficient, complex dielectric function, and electronic parameters like bandgap and charge carrier mobility is essential [20,21]. The physical parameters of EPPbI₃ that are pertinent to PV applications were examined in this work. Using BoltzTrap computer code [22], we have calculated thermoelectric (TE) properties such as, the effects of chemical potential and carrier concentration on electrical and thermal Conductivity (EC and TC) at different temperatures were investigated, which helped us in determining the doping level for the best PCE. The thermodynamic (TD) properties computed with Gibbs simulation code [23] also shed light on the stability of the material.

We also performed simulations of solar cell performance by using

EPPbI₃ as PVA material with SCAPS-1D [24,25]. This was the first time that a complete evaluation of most of these properties of EPPbI₃ perovskite that are pertinent to PVA layer material was conducted. The current study could inspire researchers to conduct thorough experimental studies in quest of PVA materials that are stable, economical, and environmentally friendly.

2. Computational parameters

Here, the simulation software WIEN-2k and the PBE-GGA exchange-correlation potential were used in conjunction with the density functional theory (DFT) to calculate different parameters [26–30]. In this method, a unit cell of the material was assumed to consist of two regions: a spherical space surrounding each atom, known as a muffin-tin sphere (MTS), and an interstitial region between these muffin-tin spheres. The optimized radii of the muffin-tin sphere (RMT) of Pb and I are 2.50 a.u. each and the RMTs of P, C and H were 1.50, 1.41 and 0.76 a.u., respectively. We used $5 \times 5 \times 5$ k-mesh with uniform distribution of k-points in the whole Brillouin zone (BZ) and $(\text{RMT})_{\min} \bullet K_{\max} = 3.0$. We considered the energy difference of -6 Ry between the core and valence electronic states. The Fourier expansions of the potential function and charge density with $G_{\max} = 20$ were considered. We considered the spread of atomic wave function with l values between 0 and 10 within the MTS around the atom. The SCF iterations were performed until the total energy and total charge in the unit cell converged to 10^{-4} Ry and 10^{-3} e, respectively. For the calculations of optical, TD, and TE characteristics, we used a denser k-mesh of 10000 k-points in FBZ. We used the BoltzTrap code [17] to calculate the TE parameters by varying the carrier density in the range 10^{16} – 10^{19} cm $^{-3}$ at ambient pressure and temperature.

3. Results and discussion

3.1. Structural properties

The most stable configurations of HOIPs have cubic structures with $Pm\bar{3}m$ (no. 221) space group symmetry. The structure of the chosen material EPPbI₃ also belongs to the same space group symmetry, where the EP $^+$ and Pb $^{2+}$ ions have 12-fold and 6-fold coordination, respectively [31]. The EP $^+$, Pb $^{2+}$, and I $^-$ ions have Wyckoff positions at (1/2, 1/2, 1/2), (0, 0, 0), and (0, 0, 1/2), respectively. Fig. 1 depicts optimized cubic and polyhedral 3D crystal structures of EPPbI₃, where the organic cation EP $^+$ is located in the cavity formed by four PbI₆ octahedra. The Pb $^{2+}$ cation is located at the centre of the octahedron and the I $^-$ anion at its corners. Here, we used PBE-GGA XC to calculate the total energy E of unit cells each of which has a different volume V of EPPbI₃ as depicted in Fig. 2. In this plot, we fitted the curve for E as a function of V using the Birch–Murnaghan's equation of state [32].

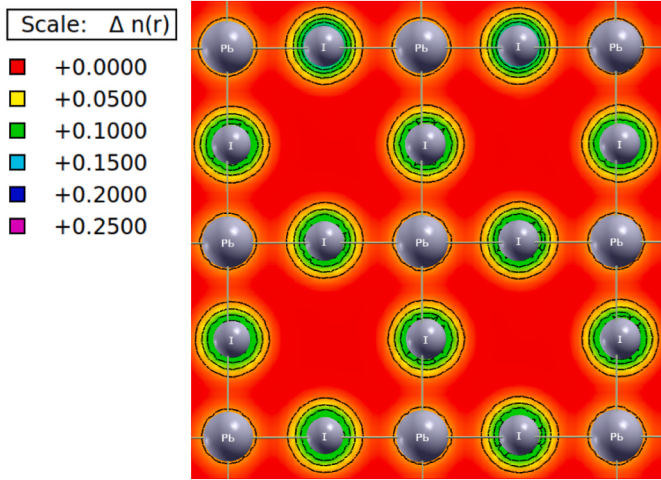


Fig. 3. The spatial variation of the charge density of valence electron in the EPPbI₃ perovskite.

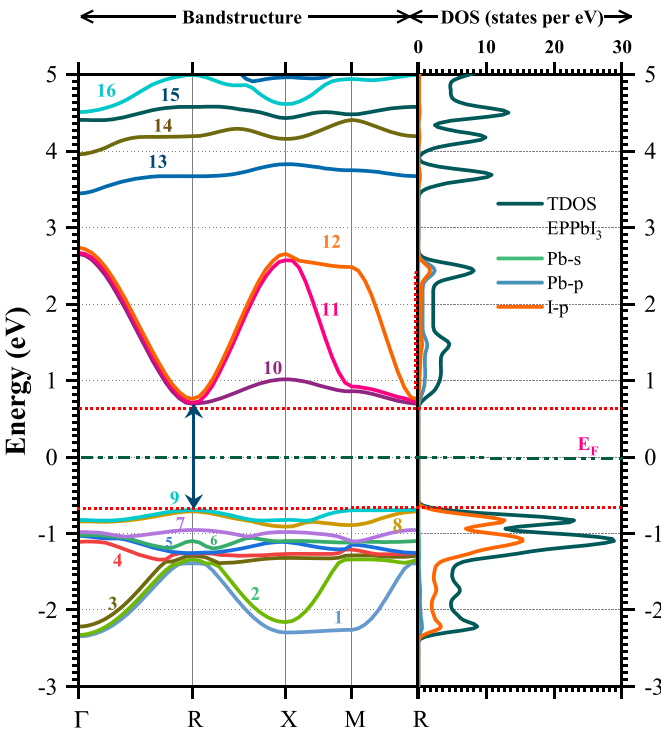


Fig. 4. The DOS and energy band structure of EPPbI₃ perovskite.

$$E(V) = E_0 + \frac{9B_0 V_0}{16} \left\{ \left[\left(\frac{V_0}{V} \right)^{2/3} - 1 \right]^3 B'_0 + \left[\left(\frac{V_0}{V} \right)^{2/3} - 1 \right]^2 \times \left[6 - 4 \left(\frac{V_0}{V} \right)^{2/3} \right] \right\}. \quad (1)$$

By using the curve fitted above, we have calculated various important physical quantities; the equilibrium lattice parameter $a = 7.40 \text{ \AA}$, the equilibrium volume of corresponding unit cell $V_0 = 405.2 \text{ \AA}^3$, the bulk modulus $B = 24.57 \text{ GPa}$, and its pressure derivative $B' = 3.40$.

3.2. Electronic properties

The spatial distribution of the electron charge density (ECD) in the unit cell of the EPPbI₃ perovskite is shown in Fig. 3 to understand the

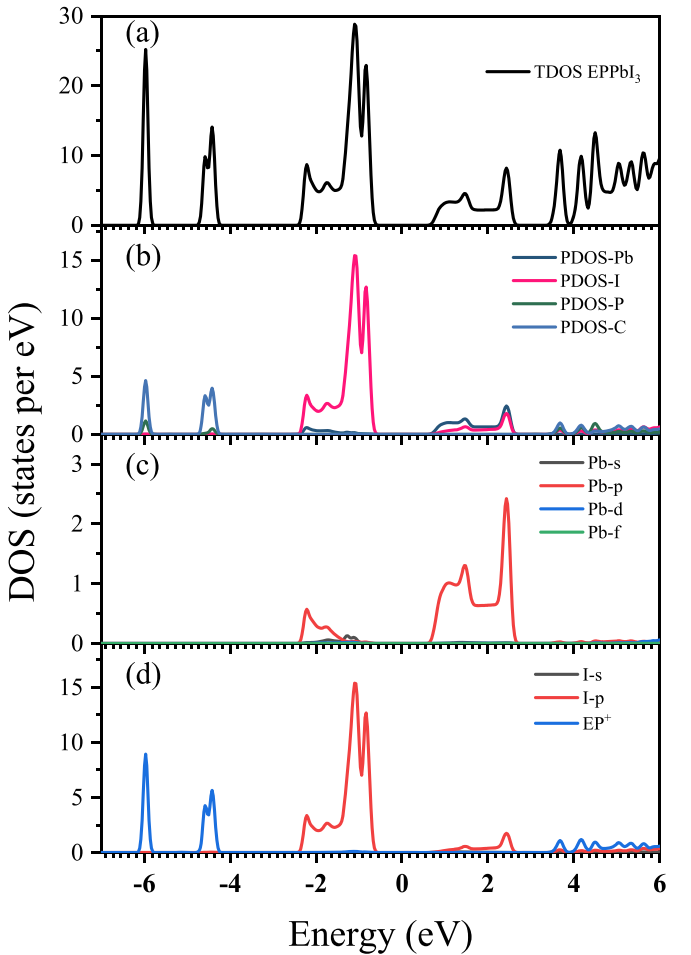


Fig. 5. The TDOS and PDOS of EPPbI₃ perovskite.

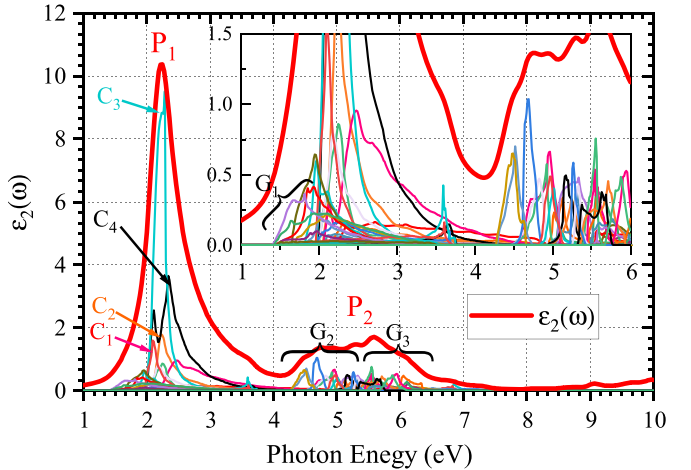


Fig. 6. The variation of Imaginary part $\epsilon_2(\omega)$ of complex dielectric function $\epsilon(\omega)$ with incident photon energy.

nature of the Pb–I bond. The ionic bonding between Pb²⁺ and I⁻ ions is shown by the circular contours of the valence electron density. The ECD plot of the material shows that the Pb–I bond is partly covalent and partly ionic. The substitution of P for N in CH₃CH₂NH³⁺ makes the Pb–I bond relatively more ionic and consequently enhances stability of the perovskite [1,2].

The optical and transport coefficients, and therefore the performance

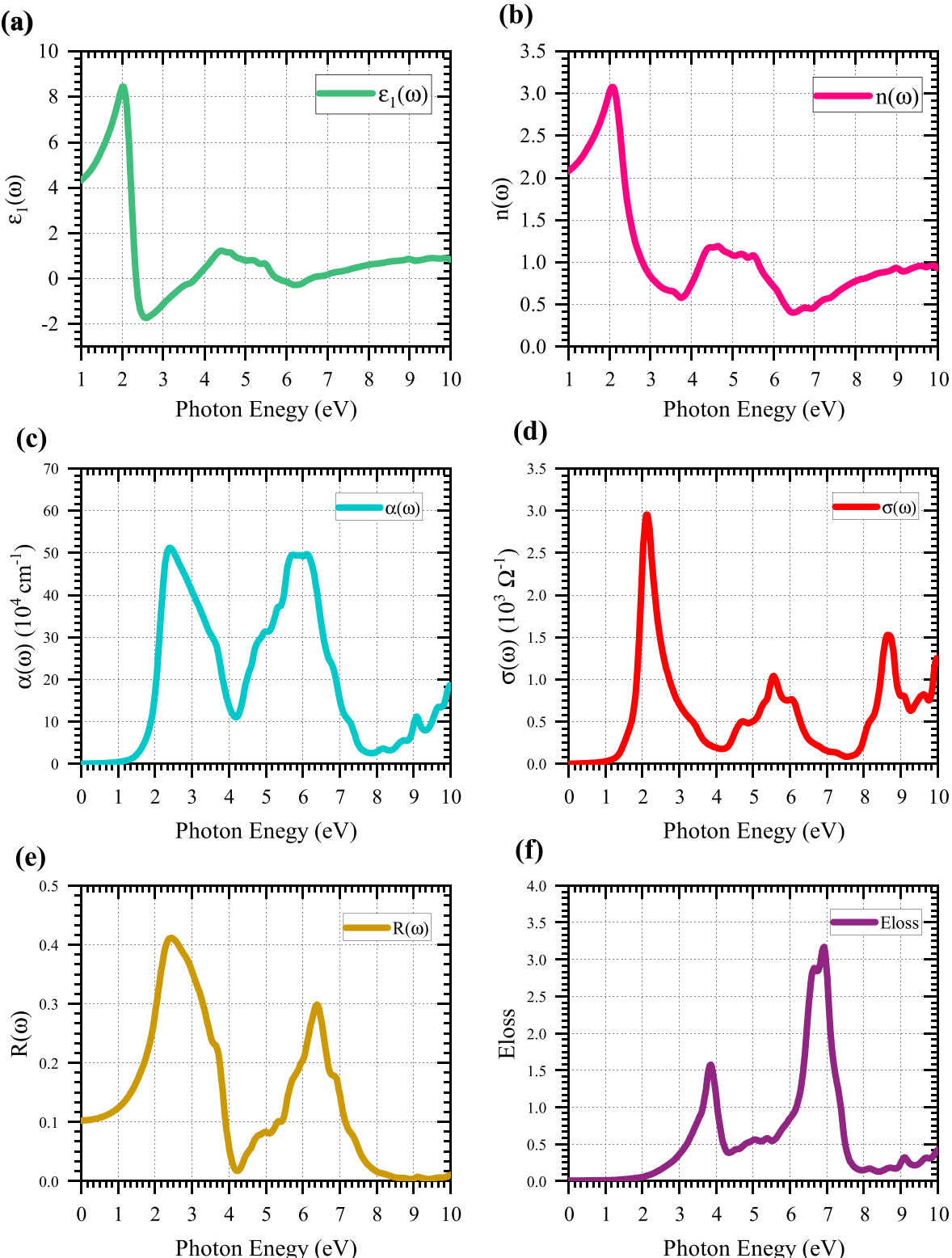


Fig. 7. The variation of (a) $\epsilon_1(\omega)$, (b) the refractive index $n(\omega)$, (c) the absorption coefficient $\alpha(\omega)$, (d) the optical conductivity $\sigma(\omega)$, (e) the reflectivity $R(\omega)$ and (f) electron energy loss function $L(\omega)$ of EPPbI₃ perovskite with incident photon energy.

of the photovoltaic devices, are largely determined by the electronic band structure (Fig. 4) and the density of states (DOS) (Fig. 5) of a material. In Fig. 4, we have depicted the band structure in FBZ with important atomic orbital level projected DOS (PDOS) plots of EPPbI₃. The energy bands numbered 1 to 9 are the VBs and the energy bands numbered 10 to 16 are the CBs. A direct forbidden energy gap of 1.388

eV appears between the VB numbered 9 and the CB numbered 10 at the high symmetry point R in the FBZ. The total DOS (TDOS) and PDOS plots clearly establish that the VBs numbered 1 through 8 are the I-5p bands, while the CB 10 evolves due to the overlapping of Pb-6s with I-5p orbitals. Here, the bands numbered 10, 11, and 12 are primarily the Pb-6p bands, while the mutual interactions of ions in unit cell produces bands

Table 1

The component peak (C_n) or group of the component peaks (G_n), the electronic transitions behind the origin of these peaks and the positions on the energy axis in DOS plot (Fig. 6).

Component peak	Electronic transition from (VB number) → (CB Number)	Peak position (eV)
G_1	7, 8, 9 → 10, 11, 12	0 to 1.38
C_1	5 → 10	2.12
C_2	2 → 10	2.22
C_3	4 → 10	2.25
C_4	3 → 10	2.34
G_2	6, 7, 8, 9 → 13, 14, 15	4.35 to 5.3
G_3	6, 7, 8, 9 → 16, 17	5.31 to 6.22

numbered 13 through 16. The forbidden energy gap in the EPPbI₃ is attributed to the interaction amongst the Pb-6s, Pb-6p, and I-5p orbitals. Fig. 5 makes it very evident that the EP⁺ ion, which resides in octahedral cavity, does not have significant DOS near the VB and CB edges.

Evidently, the calculated direct energy gap of 1.388 eV in EPPbI₃ is in the range desirable for high PCE [33]. The EPPbI₃ perovskite belongs to the family of HOIP materials with APbI₃ crystal structure. It is well established that the energy gap in APbI₃ predicted by the PBE-GGA exchange-correlation potential is very close to the experimentally observed [24–36]. This motivated us to choose PBE-GGA as the exchange-correlation potential in the present study to calculate various properties.

In order to achieve a high PCE value, the absorber material of PV cells must have a low effective mass of carriers because this will make them more delocalized and promote their wave-like transport [37]. The

hole effective mass $m_h^* = 1.014 m_e$ is calculated from the VB maxima by fitting a parabola at point R on the band structure plot (Fig. 4) and similarly, the electron effective mass $m_e^* = 0.240 m_e$ is calculated from the CB minima [38]. Obviously, the EPPbI₃ perovskite has heavier carriers than that in silicon ($m_h^* = 0.53 m_e$, $m_e^* = 0.19 m_e$) and heavier holes and lighter electrons than those in MAPbI₃ ($m_h^* = 0.12 m_e$ and $m_e^* = 0.50 m_e$) [39].

At the atomic level, we calculated the total DOS (TDOS) of EPPbI₃ and the projected DOS (PDOS) caused by the organic cation EP⁺ and the C, I, and S atoms. In addition, we also computed the PDOS for the s, p, d, and f orbitals of these atoms and plotted them in Fig. 5. These plots show that there exists an energy gap of 1.388 eV, which confirms the semiconducting nature of the material. The VB states that exist from -3 eV to the Fermi energy are caused by the hybridization of the I-5p and Pb-6s orbitals. The I-5p and Pb-6p states overlap and form the CB. The substitution of organic ion CH₃CH₂PH³⁺ in place of ion CH₃NH³⁺ or CH₃CH₂NH³⁺ has no significant impact on DOS in range from -3 eV to 3 eV, while the energy gap is slightly reduced, which makes it even more suitable for use in PV cells [1,2].

3.3. Optical properties

This section focuses on the radiation's interactions with EPPbI₃ perovskite and how such interactions change the material's optoelectronic characteristics. The performance of the device using the PVA layer of such materials depends greatly on these characteristics. The optical coefficients of EPPbI₃ that we have plotted in Figs. 6–7 are calculated in terms of the complex dielectric function $\epsilon(\omega)$ defined as

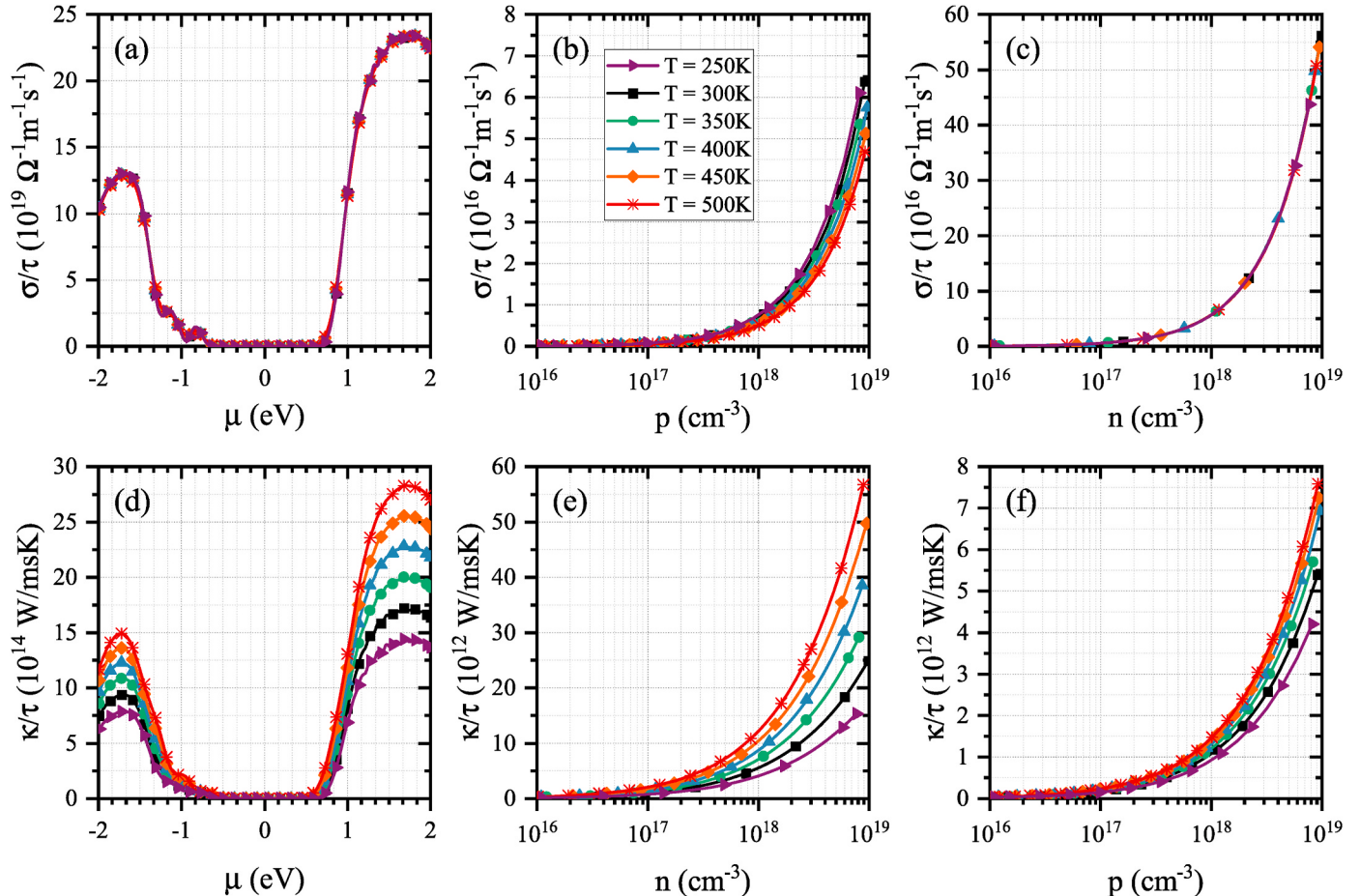


Fig. 8. The dependence of the ratios σ/τ (fig. a, b and c), κ/τ (fig. d, e and f) on (i) μ the chemical potential, (ii) n the electron concentration and (iii) p the hole concentration.

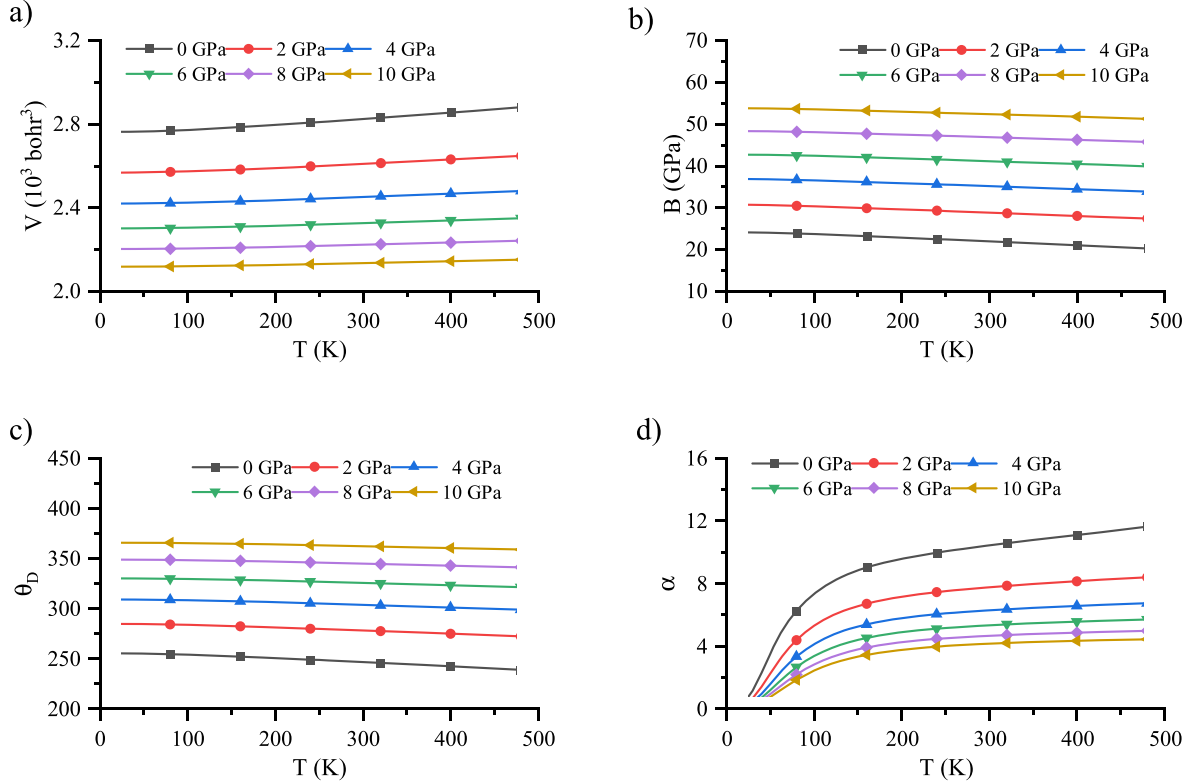


Fig. 9. The dependence of (a) Volume, (b) Bulk modulus, (c) Debye temperature, (d) Thermal expansion coefficient on temperature while the pressures are kept constant.

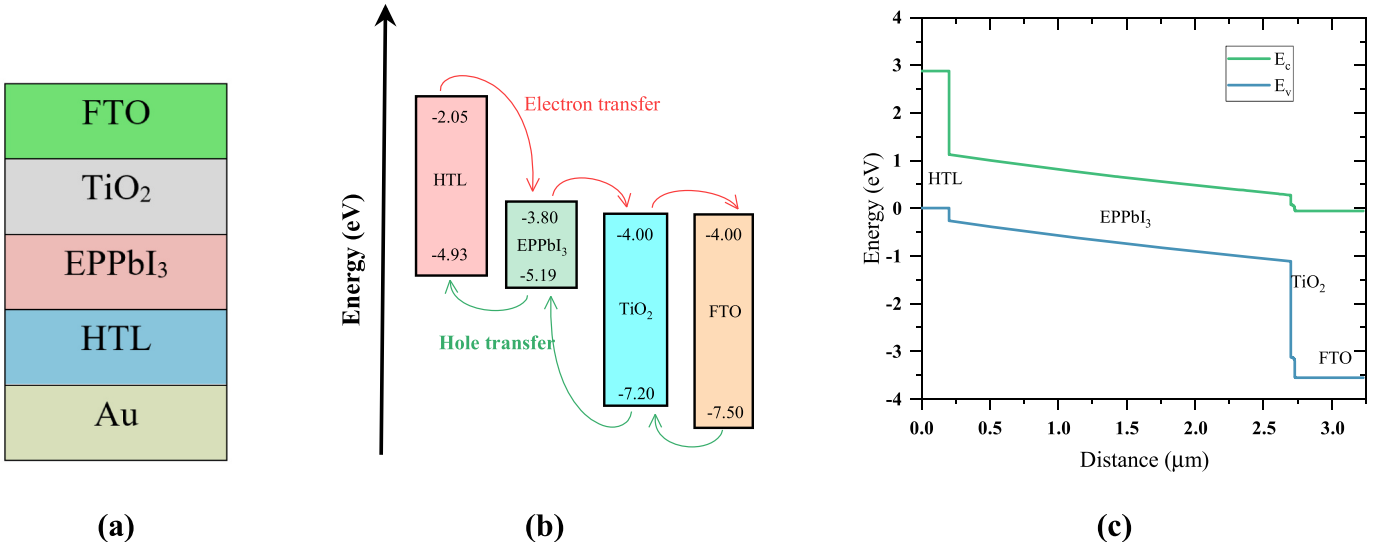


Fig. 10. The structure of PV cell (a) Layers, (b) Energy band diagram before simulation (c) Energy band diagram after simulation.

[40]

$$\epsilon(\omega) = \epsilon_1(\omega) + i\epsilon_2(\omega),$$

where $\epsilon_1(\omega)$ and $\epsilon_2(\omega)$ denote the respective real and imaginary components of complex permittivity $\epsilon(\omega)$. By assessing $\epsilon(\omega)$, it is possible to estimate how the material responds to the incident radiation. In this simulation code, the dipole matrix elements $\langle i|M|j \rangle$ are calculated for every possible combination of the i th initial VB state with energy E_i and the j th CB state with energy E_f . Then $\epsilon_2(\omega)$ is calculated using the expression [41,42]

$$\epsilon_2(\omega) = \frac{4e^2\pi^2}{\omega^2 m^2} \sum_{ij} \int |\langle i|M|j \rangle|^2 f_i(1-f_i) X \delta(E_f - E_i - \hbar\omega_0) d^3 k, \quad (3)$$

in which f_i is the Fermi function. In order to surmount the bandgap at the k point, an incident photon must have energy more than its threshold value $\hbar\omega_0$, which is represented by the quantity $(E_f - E_i - \hbar\omega_0)$. Fig. 6 displays the dependence of the $\epsilon_2(\omega)$ and its components $\{\epsilon_2(\omega)\}_{i,j}$ on the energy $\hbar\omega$ of the incident photon. Here, $\{\epsilon_2(\omega)\}_{i,j}$ are the contribution to $\epsilon_2(\omega)$ arising due to direct interband transition from the i th energy state of the VB to the j th energy state of the CB. The minimum

Table 2
Different materials' layer parameters [49] used in simulation.

Parameters	Unit	FTO	TiO ₂	EPPbI ₃	Spiro-OMeTAD
Thickness	μm	0.5	0.03	2.5	0.2
Bandgap	eV	3.5	3.200	1.388	2.880
Electron affinity	eV	4.0	4.0 [52]	3.8	2.05 [55]
Relative dielectric permittivity		9.0	9.0 [53]	4.1	3.0
Effective density of CB electrons	cm ⁻³	2.2 × 10 ¹⁸ [51]	2.2 × 10 ¹⁸	1 × 10 ¹⁸	2.2 × 10 ¹⁸
Effective density of VB holes	cm ⁻³	1.8 × 10 ¹⁹	1.8 × 10 ¹⁹	1 × 10 ¹⁸	1.8 × 10 ¹⁹
Electron mobility	cm ² /V	20	20 [51]	50 [50]	2.0 × 10 ⁻⁴
Hole mobility	cm ² /V	10	10 [51]	50 [50]	2.0 × 10 ⁻³
Shallow donor density N _D	cm ⁻³	2.0 × 10 ¹⁹	9.0 × 10 ¹⁶	1.0 × 10 ¹⁸	—
Shallow Acceptor density N _A	cm ⁻³	—	—	1.0 × 10 ¹⁸	2.0 × 10 ¹⁹
					[51]

Table 3
Defect density at interfaces/in absorber.

Interface/absorber	Spiro-OMeTAD/EPPbI ₃	EPPbI ₃ /TiO ₂	EPPbI ₃
Defect type	Neutral	Neutral	Neutral
Capture cross-section for electron and holes (cm ⁻²)	1.00 × 10 ⁻¹⁵	1.00 × 10 ⁻¹⁵	1.00 × 10 ⁻¹⁵
Energetic distribution	single	Gaussian	single
Energy level with respect to E _v (eV)	0.6	0.6	0.65
Characteristic energy (eV)	0.1	0.1	0.1
Total density (cm ⁻³)	1.00 × 10 ¹²	1.00 × 10 ¹²	1.00 × 10 ¹⁵
density at peak energy (1/cm ² .eV)	—	5.64 × 10 ¹²	—

value of photon energy necessary for the onset of $\epsilon_2(\omega)$ can be used to determine the optical forbidden band, which is shown to be around 1.388 eV in Fig. 6.

In Fig. 6, P₁ and P₂ denote the two characteristic peaks in the $\epsilon_2(\omega)$ spectrum. A further resolution of P₁ reveals its components (Table 1) labeled as C₁ to C₄. We have also analysed these component peaks with the help of band structure plot (Fig. 4) and DOS plot (Fig. 5), and tabulated the key findings in Table 1. It can be clearly inferred that the characteristic peak P₁ is created by the direct electronic band transitions from the VB states 6 through 9 to CB states 10 through 12 at the R point in FBZ, while the other broad peak P₂ is associated with the transitions from the VB states 6–9 to the CB states 13–17 at the same R point.

By using the Kramers-Kronig transformation equation, the real component $\epsilon_1(\omega)$ of the $\epsilon(\omega)$ is computed in terms of the principal value P and $\epsilon_2(\omega)$ [1,41] through the relation:

$$\epsilon_1(\omega) = 1 + \frac{2}{\pi} P \int_0^\infty \frac{\omega' \epsilon_2(\omega')}{\omega'^2 - \omega^2} d\omega'. \quad (4)$$

Now, we can use standard relations [2,43] to calculate important optical parameters in terms of $\epsilon_1(\omega)$ and $\epsilon_2(\omega)$. Fig. 7 shows the dependence of $\epsilon_1(\omega)$, refractive index $n(\omega)$, absorption coefficient $\alpha(\omega)$, optical reflectivity $R(\omega)$, optical conductivity $\sigma(\omega)$, and energy loss function $L(\omega)$ on the incident photon energy.

Fig. 7(a) and (b) illustrate the dependence of the $\epsilon_1(\omega)$ and the refractive index $n(\omega)$ on the incident photon energy. From the graphs, we can determine the two important parameters widely used in material science; the static dielectric constant $\epsilon(\omega)$ i.e., $\epsilon_1(\omega \rightarrow 0)$ and the static refractive index $n(0)$ i.e., $n(\omega \rightarrow 0)$. Which come out to be 4.37 and 2.88,

respectively. From these plots, one can deduce that $n(\omega)$ spectra follow the pattern of $\epsilon_1(\omega)$ curve. The values of both the parameters $\epsilon_1(\omega)$ and $n(\omega)$ increase and attain the respective maximum values of 8.45 and 3.7 at 2.05 eV. Afterwards, they decrease abruptly; $\epsilon_1(\omega)$ becomes negative at 2.35 eV and $n(\omega)$ falls below unity at 2.8 eV, indicating strong reflection of the incident photons having energy more than 2.8 eV. This can also be confirmed from the spike in optical reflectivity $R(\omega)$ (Fig. 7(e)) at 2.4 eV energy of incident photon. Then, in the range of photon energy from 4.36 eV to 5.56 eV again the value of both $\epsilon_1(\omega)$ and $n(\omega)$ build up and form a broader peak. Following this, both begin to diminish again and eventually the $\epsilon_1(\omega)$ approaches zero and $n(\omega)$ attains values below unity.

The absorption coefficient $\alpha(\omega)$ of a material measures radiation absorption per unit length. It usually increases as the density of CB electrons increases. Fig. 7(c) provides an illustration of how $\alpha(\omega)$ is dependent on the incident photon energy. On smoothly varying the energy of incident photon from red (1.8 eV) to green (2.43 eV), the absorption coefficient $\alpha(\omega)$ increases from $3.98 \times 10^4 \text{ cm}^{-1}$ to $5.11 \times 10^5 \text{ cm}^{-1}$ followed by sharp decrease till $3.59 \times 10^5 \text{ cm}^{-1}$ for violet (3.1 eV) photon. In the UV region, $\alpha(\omega)$ again rises sharply to the order of 10^6 cm^{-1} . The value of $\alpha(\omega)$ remains above 10^5 cm^{-1} for majority of visible portion of the solar spectrum. This is due to electron transitions from VB (I-5p and Pb-6s bands) states to CB (Pb-6p and I-5p bands) states. Clearly, the EPPbI₃ perovskite is undoubtedly a potential candidate material for PV applications due to its high absorption coefficient in visible and UV regions.

The optical conductivity $\sigma(\omega)$ of a material is an indicator of how well the material conducts solar radiation-generated electrons. Fig. 7(d) depicts the dependence of $\sigma(\omega)$ on the incident photon energy. The value of $\sigma(\omega)$ starts to build up as soon as soon as the photon energy surmounts the energy gap of 1.38 eV and eventually maximizes to $2.89 \times 10^3 \text{ cm}^{-1}$ at 2.16 eV. Fig. 7(e) illustrates the optical reflectivity $R(\omega)$. It is obvious that the greatest value of $R(\omega)$ for EPPbI₃ perovskite is merely 0.4 indicating its promises as an absorber in the visible range. The energy loss function $L(\omega)$, which is depicted in Fig. 7(f), estimates the amount of energy lost by a quickly travelling electron per unit length in the material. In visible part, a modest value of $L(\omega) < 0.31$ indicates that electrons suffer low energy dissipation in EPPbI₃ perovskite.

3.4. Thermoelectric properties

To estimate temperature dependence of thermoelectric conductivity κ and electrical conductivity σ , we have used the BoltzTrap simulation algorithm [17], which is based on constant relaxation time approach. In this approach, only the electronic contribution to κ is considered and the lattice contribution is disregarded for being insignificant. The electrical conductivity σ is defined as $\sigma = ne\mu_m$ in which n represents the carrier concentration, e the electronic charge, and μ_m the mobility. The lighter carriers have higher mobility μ_m . A greater value of σ results into lesser Joule's heating and the higher value of κ ensures rapid removal of heat produced in the PVA material. Thus, the former would increase conversion efficiency and the later would provide thermal stability of the PVA material against intense light and high temperature. The dependences of σ/τ and κ/τ (τ being the relaxation time) on μ the chemical potential, n the electron concentration and p the hole concentration in the temperature range 250–500 K have been drawn in Fig. 8. To understand the variations of κ/τ and σ/τ with electron (n-type) and hole (p-type) doping levels, we have set reference level ($\mu = 0$) at the mid-point of bandgap in Fig. 8a and d. In these plots, the regions with $\mu < 0$ correspond to p-type semiconductor while those with $\mu > 0$ represent n-type semiconductor. The computed values of these parameters are found to increase exponentially for heavily doped semiconductors (n or $p > 10^{18}$) when μ varies below -0.69 eV or beyond 0.69 eV . We can further infer that the ratio σ/τ is more immune to variation in temperature than the ratio σ/τ .

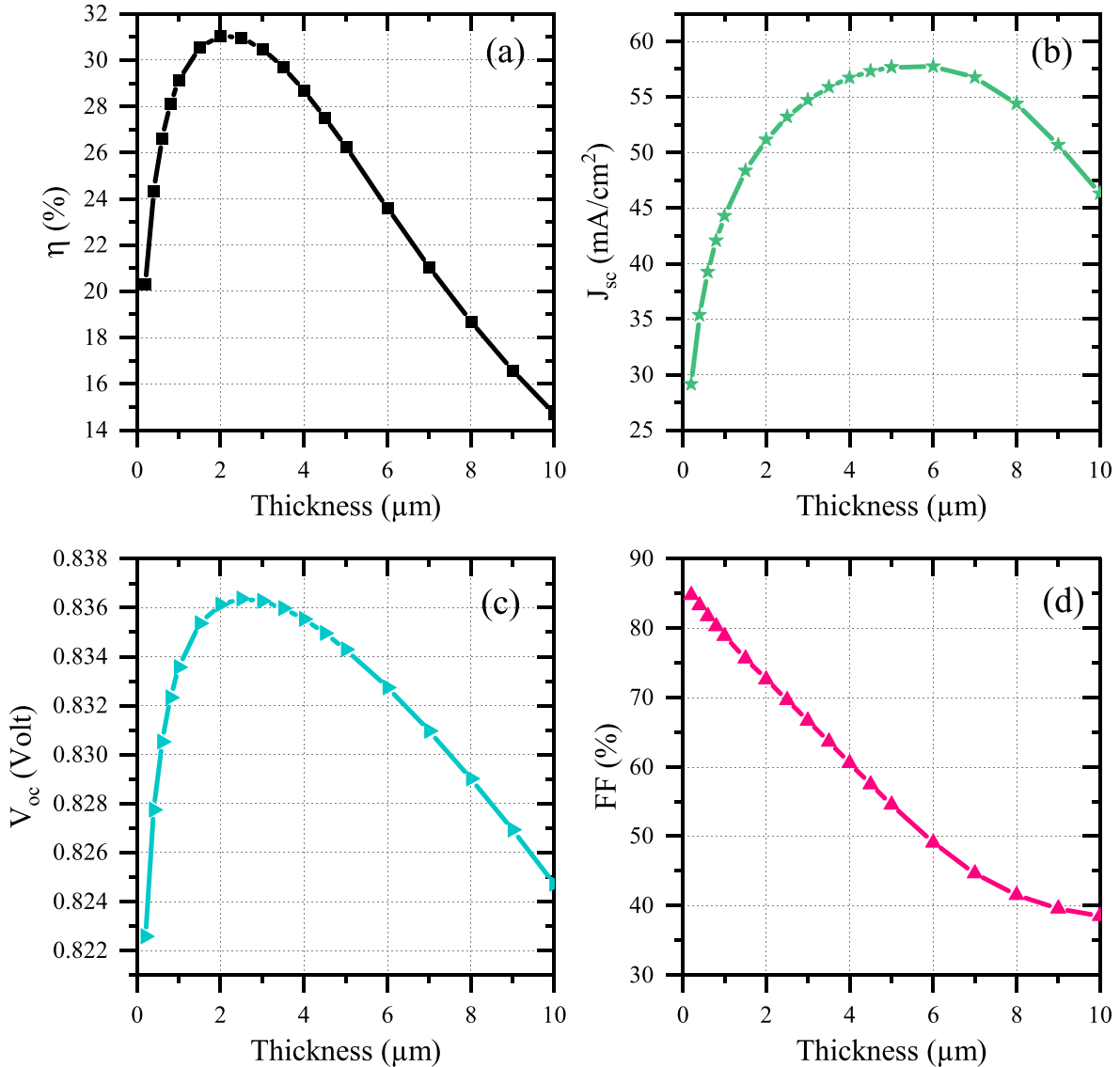


Fig. 11. The variations of solar cell parameters (a) the PCE η , (b) the short circuit current density J_{sc} , (c) the open circuit voltage V_{oc} , (d) the fill factor FF with thickness of the absorber layer.

The ratio σ/τ stays almost constant for *n*-type perovskite (Fig. 8(c)) while it decreases for *p*-type perovskite with rise in temperature (Fig. 8(b)). This suggests that the mobility and hence scattering of electrons are immune to but that of holes are susceptible to temperature variations. Furthermore, the κ/τ ratio in *n*-type material is larger than that in the *p*-type material at given temperature and concentration of carriers, indicating that the *p*-type perovskite exhibits relatively higher phonon scattering. High TC is a desirable property for an effective PVA material since it would hasten the flow of heat through an absorber layer, hence it would enhance thermal stability and improve conversion efficiency. Thus, a heavily doped *n*-type EPPbI₃ material is an ideal choice for PV applications due to its high TC, which is a desirable property of potential PVA material.

3.5. Thermal properties

The TD properties of the EPPbI₃ perovskite material were calculated in the temperature range 50–500K and pressure range 0–10 GPa by using the Gibbs programme [18]. The quasi-harmonic Debye model [18] with the standard relations [44–48] were employed in this code. The dependence of volume V and bulk modulus B on temperature T at chosen

pressures P are depicted in Fig. 9(a) and (b), respectively. The former goes up while the latter goes down with temperature, as can be seen in these plots. The material's stability is indicated by the material's high and consistent Bulk modulus B value with respect to temperature variation. Fig. 9(c) shows how the Debye temperature θ_D of the material changes with temperature at chosen pressures. The parameter θ_D is more sensitive to pressure changes than the temperature. Fig. 9(d) depicts how pressure and temperature affect the thermal expansion coefficient α . As can be seen, the parameter α is sensitive to temperature variations in the low-temperature regimes but as the temperature rises, the curve gradually flattens.

3.6. Solar cell simulation SCAPS-1d

Here, we use one-dimensional Solar Cell Capacitance Simulator (SCAPS-1d) to calculate the solar cell's characteristics, including J_{sc} , η , V_{oc} , and FF, under standard illumination of AM1.5G and 100 mW/cm² at $T = 300$ K. The SCAPS-1d has been developed at ELIS, University of Gent, and is freely available to the PV research community and can solve one-dimensional semiconductor equations in addition to the Poisson equation and the continuity equations for electrons and holes under steady-

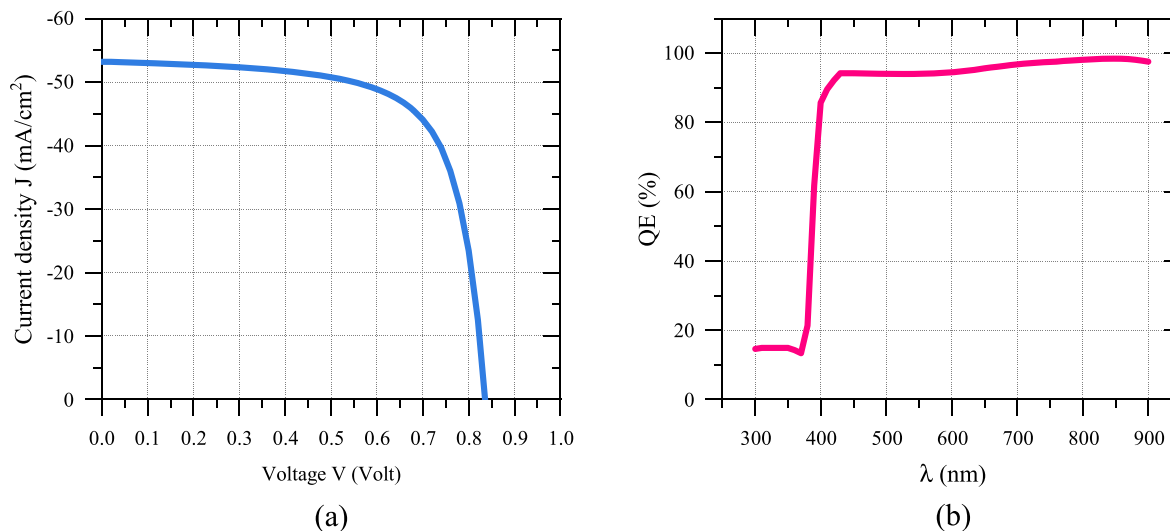


Fig. 12. (a) The J-V characteristics curve, (b) Variation of Quantum efficiency QE as a function of wavelength λ at Temperature 300 K and PVA layer of thickness 2.5 μm .

state conditions.

The architecture of a solar cell based on PVA layer of EPPbI₃ perovskite are shown in Fig. 10(a). The cell design is composed of glass substrate/FTO/ETL/PVA/HTL/Au and TiO₂ serves as electron transport layer (ETL) and Spiro-OMeTAD as the hole transport layer (HTL). The energy band diagram of the solar cell before and after device simulations are shown in Fig. 10(b) and (c), respectively.

Table 2 summarizes the fundamental characteristics of ETL, HTL, and FTO layers that were considered for our simulations were borrowed from published research work [49–56]. Other variables, such as thermal velocity of both electrons and hole, were assumed to be the same for all layers and were set at 10⁷ cm/s. Since EPPbI₃ belongs to HOIPs and is being investigated for the first time, some of the parameters were taken from other HOIPs such as MAPbI₃ and FAPbI₃. For optimized results, the EPPbI₃ based device was assumed to have intrinsic carrier density of 1.0 \times 10¹⁸ cm⁻³. The defect density within and at interfaces of the PVA layer is summarized in Table 3. The defects at ETL/PVA and PVA/HTL interfaces were considered to be single and neutral. The respective work function of back metal and FTO were set to 4.9 eV and 4.0 eV.

To investigate the performance of the solar cell based on the proposed PVA material, we simulated the power conversion efficiency (PCE) η , the short circuit current density J_{sc} , the open circuit voltage V_{oc} , and the fill factor FF as a function of thickness of the absorber layer, which are displayed in Fig. 11(a, b, c). It can be inferred that as the thickness of PVA layer increases from 200 nm the PCE η of the solar cell increases sharply to maximum value 31.8 % for the layer of thickness 2.5 μm . Thereafter, η gradually attenuates. The maximum possible current density J_{sc} (58 mA/cm²) can be obtained for PVA layer of thickness 6 μm . The open circuit voltage V_{oc} replicates the variation pattern of η and maximizes at 0.836 V. The fill factor FF of the proposed solar cell decreases smoothly as the thickness of PVA layer increases.

Obviously, a solar cell with a PVA film of thickness 2.5 μm gives the best performance. Therefore, we have considered PVA layer of thickness 2.5 μm (Table 2) for further simulation of Current density J - Voltage V characteristics and Quantum Efficiency (QE) and plotted them in Fig. 12.

4. Summary and conclusions

We have provided an in-depth examination of the structural, electronic, optical, thermoelectric, and thermodynamic properties of HOIP EPPbI₃ using DFT and the PBE-GGA XC potential. The key conclusions are as follows.

1. The direct bandgap of the EPPbI₃ perovskite is 1.388 eV. The ECD plot demonstrates the ionic character of the bonding between the cation Pb³⁺ and anion I⁻.
2. The static dielectric constant and static refractive index of the perovskite are determined to be 4.37 and 2.88, respectively.
3. Direct electronic transition between the valance and conduction bands is shown by the characteristic peaks in absorption spectra. It has the potential to be used as a PVA material due to its strong absorption coefficient ($> 10^4 \text{ cm}^{-1}$) in the visible region of the solar spectrum.
4. In *n*-type (*p*-type) EPPbI₃, the mobility and scattering of electrons (holes) are essentially (weakly) independent of temperature. The *n*-type EPPbI₃ perovskite has large electrical conductivity and comparatively superior heat conductivity, making it a potentially useful PVA material.
5. Using SCAPS-1d, the high value of simulated PCE (31.8%) for EPPbI₃ perovskite supports its applicability as a PVA material.
6. A PV cell made of a 2.5 μm thick *n*-type EPPbI₃ film produces an open-circuit voltage of 0.836 V and a fill factor of 68%, demonstrating the usefulness of *n*-type EPPbI₃ as an efficient PVA material.

Ethical approval

Not applicable on this work.

Funding

No funding for this work.

CRediT authorship contribution statement

Tarun Kumar Joshi: Writing – original draft, Methodology, Investigation. **Giriraj Sharma:** Visualization, Resources, Data curation, Conceptualization. **Yogita R. Sharma:** Validation, Software. **Ajay Singh Verma:** Writing – review & editing, Supervision.

Declaration of competing interest

The authors declare that they have no known competing financial interests or personal relationships that could have appeared to influence the work reported in this paper.

Data availability

Data will be made available on request.

References

- [1] T.K. Joshi, A. Shukla, G. Sharma, A.S. Verma, First-principles spectroscopic screening of hybrid perovskite ($\text{CH}_3\text{CH}_2\text{NH}_3\text{PbI}_3$) with fundamental physical properties: a potential photovoltaic absorber, *Int. J. Energy Res.* 45 (2021) 908–919.
- [2] T.K. Joshi, A. Shukla, G. Sharma, A.S. Verma, Emerging potential photovoltaic absorber hybrid halide perovskites ($\text{CH}_3\text{CH}_2\text{NH}_3\text{PbX}_3$; X = Br, Cl) materials: an ab-initio calculation, *Int. J. Energy Res.* 45 (2021) 15231–15244.
- [3] J.W. Lee, S.H. Bae, N.D. Marco, Y.T. Hsieh, Z. Dai, Y. Yang, “The role of grain boundaries in perovskite solar cells” *Materials, Today Energy* 7 (2018) 149–160.
- [4] S.M. Liu, Y.J. Cao, L. He, P.P. Shi, Q. Ye, Phosphonium-based one-dimensional perovskite showing dielectric behaviors and phase transitions, *Inorg. Chem.* 59 (2020) 18396–18401.
- [5] R. Singh, S.V. Akram, A. Gehlot, D. Buddhi, N. Priyadarshi, B. Twala, Energy System 4.0: Digitalization of the energy sector with inclination towards sustainability, *Sensors* 22 (2022) 6619.
- [6] K. Wang, D. Yang, C. Wu, M. Sanghadasa, S. Priya, Recent progress in fundamental understanding of halide perovskite semiconductors, *Prog. Mater. Sci.* 106 (2019) 100580.
- [7] U. Rani, P.K. Kamlesh, R. Agrawal, A. Shukla, A.S. Verma, Emerging study on lead-free hybrid double perovskite ($\text{CH}_3\text{NH}_3)_2\text{AgInBr}_6$: potential material for energy conversion between heat and electricity, *Energy Technol.* 10 (2022) 2200002.
- [8] Monika, S. Pachori, R. Agrawal, B.L. Choudhary, A.S. Verma, An efficient and stable lead-free organic-inorganic tin iodide perovskite for photovoltaic device: progress and challenges, *Energy Rep.* 8 (2022) 5753–5763.
- [9] C. Wehrenfennig, G.E. Eperon, M.B. Johnston, H.J. Snaith, L.M. Herz, High charge carrier mobilities and lifetimes in organolead trihalide perovskites, *Adv. Mater.* 26 (2014) 1584–1589.
- [10] S.D. Stranks, G.E. Eperon, G. Grancini, C. Menelaou, M.J.P. Alcocer, T. Leijtens, L. M. Herz, A. Petrozza, H.J. Snaith, Electron-hole diffusion lengths exceeding 1 micrometer in an organometal trihalide perovskite absorber, *Science* 342 (2013) 341–344.
- [11] G. Xing, N. Mathews, S.S. Lim, N. Yantara, X.F. Liu, D. Sabba, M. Gratzel, S. Mhaisalkar, T.C. Sum, Low-temperature solution-processed wavelength-tunable perovskites for lasing, *Nat. Mater.* 13 (2014) 476–480.
- [12] W.E.I. Sha, X. Ren, L. Chen, W.C.H. Choy, The efficiency limit of $\text{CH}_3\text{NH}_3\text{PbI}_3$ perovskite solar cells, *Appl. Phys. Lett.* 106 (2015) 221104.
- [13] A. Krishna, S. Gottis, M.K. Nazeeruddin, F. Sauvage, Mixed dimensional 2d/3d hybrid perovskite absorbers: the future of perovskite solar cells? *Adv. Funct. Mater.* 29 (2018) 1806482.
- [14] G. Abdelmaged, L. Jewell, K. Hellier, L. Seymour, B. Luo, F. Bridges, J.Z. Zhang, S. Carter, Mechanisms for light induced degradation in MAPbI_3 perovskite thin films and solar cells, *Appl. Phys. Lett.* 109 (2016) 233905.
- [15] S. Aharon, B.E. Cohen, L. Etgar, Hybrid lead halide iodide and lead halide bromide in efficient hole conductor free perovskite solar cell, *J. Phys. Chem. C* 118 (2014) 17160–17165.
- [16] H. Moatassim, A. El Kenz, A. Benyoussef, M. Loulidi, O. Mounkachi, Degradation mechanism of $\text{CH}_3\text{NH}_3\text{PbI}_3$ and enhancing its optical absorption through variety of doping sites, *Computational Condensed Matter* 29 (2021) e00611.
- [17] M. Ouafi, B. Jaber, L. Atourki, R. Bekkari, L. Laanab, Improving UV stability of MAPbI_3 perovskite thin films by bromide incorporation, *J. Alloys Compd.* 746 (2018) 391–398.
- [18] K. Ouassoul, A.E. Kenz, M. Loulidi, A. Benyoussef, M. Azzouz, Effect of orientation of the cation CH_3NH_3^+ on exciton's mobility in $\text{CH}_3\text{NH}_3\text{PbI}_3$, *Chin. J. Phys.* 80 (2022) 34–45.
- [19] F. El-Mellohi, E.T. Bentria, S.N. Rashkeev, S. Kais, F.H. Alharbi, Enhancing intrinsic stability of hybrid perovskite solar cell by strong, yet balanced, electronic coupling, *Sci. Rep.* 6 (2016) 30305.
- [20] Q. Chen, N.D. Marco, Y.M. Yang, T. Song, C. Chen, H. Zhao, Z. Hong, H. Zhou, Y. Yang, Under the spotlight: the organic-inorganic hybrid halide perovskite for optoelectronic applications, *Nano Today* 10 (2015) 355–396.
- [21] D. Liu, Q. Li, K. Wu, Ethylammonium as an alternative cation for efficient perovskite solar cells from first-principles calculations, *RSC Adv.* 9 (2019) 7356.
- [22] G.K. Madsen, D.J. Singh, BoltzTrap, a code for calculating band structure dependent quantities, *Comput. Phys. Commun.* 175 (2006) 67–71.
- [23] M.A. Blanco, A. Martín Pendás, E. Francisco, J.M. Racio, R. Franco, Thermodynamical properties of solids from microscopic theory: applications to MgF_2 and Al_2O_3 , *J. Mol. Struct. Theochem* 368 (1996) 245.
- [24] M. Burgelman, P. Nollet, S. Degrave, Modelling polycrystalline semiconductor solar cells, *Thin Solid Films* 361–362 (2000) 527–532.
- [25] M. Burgelman, K. Decock, S. Khelifi, A. Abass, Advanced electrical simulation of thin film solar cells, *Thin Solid Films* 535 (2013) 296–301.
- [26] W. Kohn, L.J. Sham, Self-consistent equations including exchange and correlation effects, *Phys. Rev.* 140 (1965) A1133–A1138.
- [27] P. Hohenberg, W. Kohn, Inhomogeneous electron gas, *Phys. Rev.* 136 (1964) B864–B871.
- [28] P. Blaha, K. Schwarz, P. Sorantin, S. Trickey, Full-potential, linearized augmented plane wave programs for crystalline systems, *Comput. Phys. Commun.* 59 (1990) 399–415.
- [29] P. Blaha, K. Schwarz, F. Tran, R. Laskowski, G.K.H. Madsen, L.D. Marks, WIEN2k: an APW+lo program for calculating the properties of solids, *J. Chem. Phys.* 152 (2020) 074101.
- [30] J.P. Perdew, K. Burke, M. Ernzerhof, Generalized gradient approximation made simple, *Phys. Rev. Lett.* 77 (1996) 3865–3868.
- [31] S. Pachori, R. Agrawal, A. Shukla, A.S. Verma, First-principles calculations for fundamental and spectroscopic screening of hybrid perovskite ($\text{HC}(\text{NH}_2)_2\text{PbI}_3$) formamidinium lead iodide, *Mater. Chem. Phys.* 287 (2022) 126149.
- [32] F.D. Murnaghan, On the theory of the tension of an elastic cylinder, *Proc. Natl. Acad. Sci. USA* 30 (1944) 382–384.
- [33] W. Shockley, H.J. Queisser, “Detailed balance limit of efficiency of p-n junction solar cells” *J. Appl. Phys.* 32 (1961) 510–519.
- [34] F. Hao, C.C. Stoupios, R.P.H. Chang, M.G. Kanatzidis, Anomalous bandgap behavior in mixed Sr and Pb perovskites enables broadening of absorption spectrum in solar cells, *J. Am. Chem. Soc.* 136 (2014) 8094–8099.
- [35] C. Lee, J. Hong, A. Stroppa, M.H. Whangbo, J.H. Shim, Organic inorganic hybrid perovskites ABI_3 ($\text{A} = \text{CH}_3\text{SH}_3$, NH_2CHNH_2 ; $\text{B} = \text{Sn, Pb}$) as potential thermoelectric materials: a density functional evaluation, *RSC Adv.* 5 (2015) 78701–78707.
- [36] E. Tenuta, C. Zheng, O. Rube, Thermodynamic origin of instability in hybrid halide perovskites, *Sci. Rep.* 6 (2016) 37654.
- [37] N. Park, Methodologies for high efficiency perovskite solar cells, *Nano Convergence* 3 (2016) 15.
- [38] J. Yang, M. Meissner, T. Yamaguchi, X. Zhang, T. Ueba, L. Cheng, S. Ideta, K. Tanaka, X. Zeng, N. Ueno, S. Kera, Band dispersion and hole effective mass of methylammonium lead iodide perovskite, *Sol. RRL* 2 (2018) 1800132.
- [39] C. Motta, F. El-Mellohi, S. Sanvitto, Charge carrier mobility in hybrid halide perovskites, *Sci. Rep.* 5 (2015) 12746.
- [40] U. Rani, P.K. Kamlesh, R. Agarwal, J. Kumari, A.S. Verma, Electronic and thermophysical properties of double antiperovskites X_6SO_4 ($\text{X} = \text{Na, K}$ and $\text{A} = \text{Cl, Br, I}$): a non-toxic and efficient energy storage materials, *Int. J. Quant. Chem.* 121 (2021) e26759.
- [41] U. Rani, Y. Soni, P.K. Kamlesh, S. Pachori, A.S. Verma, Fundamental theoretical design of Na-ion and K-ion based double antiperovskite X_6SO_4 ($\text{X} = \text{Na, K}$; $\text{A} = \text{Cl, Br, I}$ and halides: potential candidate for energy storage and harvester, *Int. J. Energy Res.* 45 (2021) 13442–13460.
- [42] Pallavi, C. Singh, P.K. Kamlesh, K. Kaur, A.S. Verma, Nowotny-Juza phase KBeX ($\text{X} = \text{N, P, As, Sb, and Bi}$) half-Heusler compounds: applicability in photovoltaics and thermoelectric generators, *J. Mol. Model.* 29 (2023) 23.
- [43] T.K. Joshi, A. Shukla, G. Sharma, A.S. Verma, Computational determination of the physical properties of ethyl-ammonium germanium iodide ($\text{CH}_3\text{CH}_2\text{NH}_3\text{GeI}_3$): an emerging material for photovoltaic cell, *Mater. Chem. Phys.* 251 (2020) 123103.
- [44] M.A. Blanco, A. Martín Pendás, E. Francisco, J.M. Racio, R. Franco, Thermodynamical properties of solids from microscopic theory: applications to MgF_2 and Al_2O_3 , *J. Mol. Struct. Theochem* 368 (1996) 245.
- [45] M. Flórez, J.M. Recio, E. Francisco, M.A. Blanco, A.M. Pendás, First-principles study of the rock salt–cesium chloride relative phase stability in alkali halides, *Phys. Rev.* (2002) 144112, B 66.
- [46] E. Francisco, M.A. Blanco, G. Sanjurjo, “Atomistic simulation of SrF_2 polymorphs”, *Phys. Rev.* (2001) 094107, B 63.
- [47] J.P. Poirier, Introduction to the physics of Earth's interior, Cambridge University Press, Oxford (2000) 39.
- [48] R. Hill, “The elastic behaviour of a crystalline aggregate”, *Proc. Phys. Soc. Lond.* A65 (1952) 349.
- [49] S. Abdelaziz, A. Zekry, A. Shaker, M. Abouelatta, Investigating the performance of formamidinium tin-based perovskite solar cell by SCAPS device simulation, *Opt. Mater.* 101 (2020) 109738.
- [50] S. Karthick, S. Velumani, J. Bouclé, Experimental and SCAPS simulated formamidinium perovskite solar cells: a comparison of device performance, *Sol. Energy* 205 (2020) 349–357.
- [51] D. Hui-Jing, W. Wei-Chao, Z. Jian-Zhuo, Device simulation of lead-free $\text{CH}_3\text{NH}_3\text{SnI}_3$ perovskite solar cells with high efficiency, *Chin. Phys. B* 25 (10) (2016) 108802.
- [52] A. Niemegeers, M. Burgelman (Eds.), “Numerical Modelling of AC-Characteristics of CdTe and CIS Solar Cells”, Conference Record of the Twenty Fifth IEEE Photovoltaic Specialists Conference, 1996, pp. 13–17.
- [53] M.D. Stamate, On the dielectric properties of dc magnetron TiO_2 thin films, *Appl. Surf. Sci.* 218 (1) (2003) 318–323.
- [54] Evaluation of new materials for electron and hole transport layers in perovskite based solar cells through SCAPS-1D simulations, in: S. Bansal, P. Aryal (Eds.), IEEE 43rd Photovoltaic Specialists Conference, PVSC June, 2016, pp. 5–10.
- [55] D. Poplavskyy, J. Nelson, Nondispersive hole transport in amorphous films of methoxy-spirofluorene-arylamine organic compound, *Appl. Phys.* 93 (1) (2003) 341–346.
- [56] D. Liu, T.L. Kelly, Perovskite solar cells with a planar heterojunction structure prepared using room-temperature solution processing techniques, *Nat. Photonics* 8 (2013) 133.